

## Electronic Supplemental Information

Magnetic and magnetocaloric properties of two  $Gd^{3+}Fe^{3+}_4$  metallacrowns and a comparison to other magnetic metallacrown topologies

Elvin V. Salerno,<sup>a</sup> Jeff W. Kampf,<sup>a</sup> Vincent L. Pecoraro,<sup>a</sup> and Talal Mallah<sup>b</sup>

<sup>a</sup>*Department of Chemistry, University of Michigan, Ann Arbor, Michigan, 48108, USA*

<sup>b</sup>*Institut de Chimie Moléculaire et des Matériaux d'Orsay, CNRS, Université Paris-Saclay, 91405 Orsay Cedex, France.*

### Contents

Table S1. Crystal data and structure refinement for complex <b>2</b> .....	3
Detailed Structural Considerations. ....	4
Figure S1 Unit cell composition for complex <b>1</b> viewed along the a-, b-, and c- axes.....	6
Figure S2 Multiple views of complex <b>1</b> .....	6
Figure S3 View of two isomers of <b>1</b> (top) and <b>2</b> (bottom).....	7
Figure S4 $\Lambda/\Delta$ helical assignments for complex <b>1</b> for each of the four irons in each isomer. ....	8
Figure S5 Unit cell composition for complex <b>2</b> viewed along the a-, b-, and c- axes.....	9
Figure S6 Four views of complex <b>2</b> .....	9
Figure S7 $\Lambda/\Delta$ helical assignments for complex <b>2</b> for each of the four irons in each isomer. ....	10
Table S2 Measurements concerning the primary $Gd^{3+}$ coordination sphere distances .....	10
Table S3 Measurements concerning the primary $Fe^{3+}$ coordination sphere distances .....	11
Figure S8 Comparison of experimental magnetization data for <b>1</b> and <b>2</b> at 2K.....	11
Figure S9 Fit of the temperature dependent magnetization data for <b>1</b> from 0-7 T, 2-20 K.....	12
Figure S10 Attempted fit of the temperature dependent magnetization data for <b>2</b> .....	12
Figure S11 Temperature dependent magnetic entropy change (per mole) .....	13
Figure S12 Energy levels determined via fitting the spin Hamiltonian to the data for <b>1</b> .....	13
Calculating the magnetic entropy at 2K.....	13
Figure S13 Simulation of the energy levels of $Fe^{3+}[9-MC_{Fe^{III}N(shi)}-3]-1$ .....	14
Figure S14 Simulation of the magnetic susceptibility of the complex $Fe^{3+}[9-MC_{Fe^{III}N(shi)}-3]-2$ .....	15
Figure S15 Simulation of the energy levels of $Fe^{3+}[9-MC_{Fe^{III}N(shi)}-3]-2$ with ZFS .....	15
Figure S16 Simulation of the energy levels of $Fe^{3+}[9-MC_{Fe^{III}N(shi)}-3]-2$ with zJ .....	16
Figure S17 Simulation of the energy levels of $Cu^{2+}[12-MC_{Fe^{III}N(shi)}-4]$ .....	16
Figure S18 Lower portion of the Energy diagram for the spin states of $Cu^{3+}Fe^{3+}_4$ .....	17
Figure S19 Lower portion of the Energy diagram for the spin states of $Ni^{2+}Fe^{3+}_4$ .....	17
Figure S20 Lower portion of the Energy diagram for the spin states of $Co^{2+}Fe^{3+}_4$ .....	18

Figure S21 Lower portion of the Energy diagram for the spin states of $\text{Mn}^{3+}\text{Fe}^{3+}_4$ .....	18
Figure S22 Lower portion of the Energy diagram for the spin states of $\text{Fe}^{3+}\text{Fe}^{3+}_4$ .....	19
References .....	19

**Table S1.** Crystal data and structure refinement for complex **2**.

Identification code	evsr53b
Empirical formula	C <sub>72</sub> H <sub>70</sub> Fe <sub>4</sub> GdN <sub>11</sub> O <sub>26</sub>
Formula Weight	1886.04
Temperature	85(2) K
Wavelength	1.54184 Å
Crystal system, space group	Orthorhombic, <i>Pbca</i>
Unit cell dimensions	$a = 15.21501(16)$ Å $\alpha = 90^\circ$ $b = 30.8930(2)$ Å $\beta = 90^\circ$ $c = 38.1360(2)$ Å $\gamma = 90^\circ$
Volume	17925.3(3) Å <sup>3</sup>
Z, calculated density	8, 1.398 mg/m <sup>3</sup>
Absorption coefficient	10.413 mm <sup>-1</sup>
<i>F</i> (000)	7640
Crystal size	0.14 x 0.04 x 0.04 mm
$\theta$ range for data collection	2.861° to 69.841°
Limiting indices	-18 ≤ <i>h</i> ≤ 16, -37 ≤ <i>k</i> ≤ 36, -45 ≤ <i>l</i> ≤ 46
Reflections collected/unique	268915 / 16817 [R(int) = 0.1273]
Completeness to $\theta = 67.679$	100.0 %
Absorption correction	Semi-empirical from equivalents
<i>Max</i> and <i>min</i> transmission	1.00000 and 0.45021
Refinement method	Full-matrix least-squares on <i>F</i> <sup>2</sup>
Data/restraints/parameters	16817 / 175 / 1191
Goodness-of-fit on <i>F</i> <sup>2</sup>	1.060
Final <i>R</i> indices [ <i>I</i> > 2σ( <i>I</i> )]	R1 = 0.0773, wR2 = 0.2082
<i>R</i> indices (all data)	R1 = 0.0918, wR2 = 0.2250
Extinction coefficient	0.00037(3)
Largest diff. peak and hole (e <sup>-</sup> Å <sup>-3</sup> )	1.232 and -0.994 e. Å <sup>-3</sup>

**Detailed Structural Considerations.** Complex **1** was described previously, but is described again here to facilitate an adequate comparison to **2**.<sup>1</sup> Complex **1** has the metal/ligand set  $\text{Fe}_4\text{Gd}(\text{shi})_4(\text{benzoate})_4(\text{pyridine})_4$  (**Figure 2**). Complex **1** is anionic, with a pyridinium counterion. This complex is a 12- $\text{MC}_{\text{Fe}^{\text{III}}(\text{N})(\text{shi})}$ -4 structure (see **Figures 1, S1, and S2**), however rather than a flat metallacrown ring one of the ligands is folded below the plane, that ligand's planar position instead occupied by two pyridine ligands. A  $\text{Gd}^{3+}$  ion fills the central cavity of the complex, bonded in a pseudo square antiprismatic  $\text{GdO}_8$  geometry with the four shi oxime oxygens binding one plane, and four benzoate oxygens filling the other plane (**Figure 2**). The  $\text{GdO}_8$  geometry is approximated by  $D_{4d}$  symmetry (**Figure 3**). The  $\text{Gd}^{3+}$  lies in the center of the metallacrown cavity, but is above the metallacrown ring plane.

The four benzoates bind the four  $\text{Fe}^{3+}$  axially at the other oxygen. Each  $\text{Fe}^{3+}$  is bonded to three shi oxygens, one shi nitrogen, one pyridine nitrogen, and one benzoate oxygen in a pseudo octahedral  $\text{FeN}_2\text{O}_4$  arrangement. Each  $\text{Fe}^{3+}$  is bonded via an Fe-N-O-Fe scheme to its two nearest  $\text{Fe}^{3+}$ . Each  $\text{Fe}^{3+}$  is bonded to the  $\text{Gd}^{3+}$  through the oxime oxygen of the shi ligand as Fe-O-Gd, and additionally via the benzoate ligand as Fe-O-C-O-Gd. All four  $\text{Fe}^{3+}$  are equivalent in terms of bonding through atoms to the  $\text{Gd}^{3+}$ . Each  $\text{Fe}^{3+}$  has identical ligand sets, however, all four  $\text{Fe}^{3+}$  are not crystallographic equivalent. The  $\text{Fe}^{3+}$  are labeled based on the distance from the  $\text{Gd}^{3+}$  ion, with the  $\text{Fe}^{3+}$ - $\text{Gd}^{3+}$  distances: Fe-1: 3.816, Fe-2: 3.759, Fe-3: 3.744 and Fe-4: 3.779 Å (**Figure 2**). Fe-1 and Fe-2 have the pyridine N bound perpendicular to the carboxylate O; while Fe-3 and Fe-4 have the pyridine N bound opposite the carboxylate O, the position opposite the carboxylate O is occupied by the shi ligand which is bent below the ring plane.

Within the crystal structure, two distinct isomeric complexes exist, which are related by an inversion center between them (**Figure S3**). When considering the shi<sup>-</sup> ligands as bidentate for each  $\text{Fe}^{3+}$  (either from hydroximate N to phenolic O sequence [N-C-C-C-O]; or hydroximate oxime O to hydroximate carbonyl O [O-N-C-O]): compound **1** has one complex with two planar  $\text{Fe}^{3+}$  configurations, one  $\Lambda$  propeller configuration, and one  $\Delta$  propeller configuration. The inversion related counterpart has two planar  $\text{Fe}^{3+}$  configurations, one  $\Delta$  propeller configuration, and one  $\Lambda$  propeller configuration, where the chiral assignments are opposite the inversion-related counterpart (**Figure S4**).

Complex **2** has the ligand set  $\text{Fe}_4\text{Gd}(\text{shi})_4(\text{H}_2\text{shi})_3(\text{pyridine})_3(\text{H}_2\text{O})$  (**Figures 2, S5, and S6**). In addition to the four tri-deprotonated shi<sup>3-</sup> ligands in the metallacrown ring, **2** also has three additional mono-deprotonated  $\text{H}_2\text{shi}^-$  ligands filling the set. This is compared to **1** which has four benzoate anions completing the set. Thus **1** is a mono-anionic complex ( $[\text{Gd}^{3+}\text{Fe}^{3+}_4\text{shi}^{3-}_4\text{Bz}^-_4]^-$ ) while **2** is neutral ( $[\text{Gd}^{3+}\text{Fe}^{3+}_4\text{shi}^{3-}_4\text{H}_2\text{shi}^-_3]$ ). All four  $\text{Fe}^{3+}$  are crystallographically inequivalent. The  $\text{Fe}^{3+}$  are labeled sequentially around the ring where Fe-1 has two pyridine N bound and Fe-2 has one pyridine N bound, and Fe-3 and Fe-4 are the next  $\text{Fe}^{3+}$  in the metallacrown ring. Complex **2** is a 12- $\text{MC}_{\text{Fe}^{\text{III}}(\text{N})(\text{shi})}$ -4 structure, however it has a bent geometry with the metallacrown ring presenting as a butterfly-type topology creasing at two opposite  $\text{Fe}^{3+}$  ions. According to the labeling scheme specified above, Fe-2 and Fe-4 represent the “body” while Fe-1 and Fe-3 represent the “wingtips” of the butterfly shape (**Figure 2**).  $\text{Fe}^{3+}$ - $\text{Gd}^{3+}$  distances for **2** are: Fe-1: 3.983, Fe-2: 3.483, Fe-3: 3.880 and Fe-4: 3.502 Å

A  $\text{Gd}^{3+}$  ion fills the central cavity of the complex, bonded in a  $\text{GdO}_8$  geometry with the four metallacrown ring shi's oxime oxygens binding one  $\text{O}_4$  plane. The other  $\text{O}_4$  plane is filled at one position by a coordinating water, as well as three oxygens from two  $\text{H}_2\text{shi}$  ligands bonding above the metallacrown ring. The  $\text{GdO}_8$  coordination resembles a square antiprism which is quite distorted on one of the planes (**Figure 3**). One  $\text{H}_2\text{shi}$  bonds the  $\text{Gd}^{3+}$  via its oxime oxygen, the other binds the  $\text{Gd}^{3+}$  via both its oxime oxygen and hydroximate carbonyl group. Each of these two  $\text{H}_2\text{shi}$  oxime oxygens is also bridging one of the  $\text{Fe}^{3+}$  occupying the position of the metallacrown ring's crease (“butterfly body”) as Fe-O-Fe. The two  $\text{Fe}^{3+}$  on the “butterfly body” have two Fe-O-Gd linkages. The other two  $\text{Fe}^{3+}$  ions, at

the “butterfly wingtip” positions, only have one Fe-O-Gd linkage. The Gd<sup>3+</sup> lies above the body of the metallacrown “butterfly.”

Each Fe<sup>3+</sup> is bonded to the Gd<sup>3+</sup> through the hydroximate oxygen of the shi ligand as Fe-O-Gd. Only two Fe<sup>3+</sup> additionally bind the Gd<sup>3+</sup> through the oxime bridge described above. The four Fe<sup>3+</sup> ions have pseudo octahedral bonding arrangements with the ligand sets Fe-1: FeO<sub>3</sub>N<sub>3</sub>, Fe-2: FeO<sub>4</sub>N<sub>2</sub>, Fe-3: FeO<sub>5</sub>N, and Fe-4: FeO<sub>5</sub>N. Any coordinating nitrogen in excess of one comes from a coordinating pyridine.

Within the crystal structure, two distinct isomeric complexes exist, which are related by an inversion center between them (**Figure S3**). When considering the shi<sup>-</sup> ligands as bidentate for each Fe<sup>3+</sup> (either from hydroximate N to phenolic O sequence [N-C-C-C-O]; or hydroximate oxime O to hydroximate carbonyl O [O-N-C-O]): compound **1** has one complex with one planar Fe<sup>3+</sup> configuration, one  $\Lambda$  propeller configuration, and two  $\Delta$  propeller configurations. As required, the inversion related counterpart has one planar Fe<sup>3+</sup> configuration, two  $\Lambda$  propeller configurations, and one  $\Delta$  propeller configuration, where the chiral assignments are opposite of the inversion-related counterpart (**Figure S7**). These local structural constraints cause the non-planar structural orientation of the molecule. They are also interesting in that prior metallacrowns that had mixtures of propeller and planar configurations had symmetric numbers of each isomer (e.g., 9-MC-3 contained either 3  $\Lambda$  or 3  $\Delta$  centers<sup>2,3</sup> whereas 15-MC-5 required  $\Lambda$ ,  $\Delta$ ,  $\Lambda$  with 2 planar centers closing the metallacrown ring<sup>4</sup> or 18-MC-6 structures that alternated  $\Lambda$  and  $\Delta$  sites<sup>5</sup>). The fact that these molecules are chiral will not intrinsically alter the magnetic properties of these complexes, however, the orientation of hydroximate ligands can have an impact on the exchange interactions differing between the two 12-MC-4 species of complexes **1** and **2**. Those that are planar, hence requiring all Fe atoms to display planar orientations of the two shi 5-membered chelate rings, will have more uniform bonding and, therefore, more uniform exchange interactions as opposed to these new structures which force the hydroximate ligands into an orthogonal orientation with respect to one another. Within the same molecule, a chemically equivalent oxygen atom will be disposed differently with respect to the other iron atoms and the central lanthanide. Thus, one may expect that the superexchange exhibited in these less symmetric (complex **2**), chiral metallacrowns may differ between each iron center within the molecule and certainly be different compared to a planar version of an iron 12-MC-4 (complex **1**).

Relevant angle and torsion measurements, as well as bond distance measurements, can be found in **Tables S2-S5**. Generally, **1** is more uniform than **2**, which is more ruffled and possesses some additional Fe-O-Gd interactions. The main difference between the two complexes is the benzoate ligands present in **1** and absent in **2**. For **1**, where benzoates are present in the synthesis, they bridge each Fe<sup>3+</sup> to the central Gd<sup>3+</sup> in an Fe-O-C-O-Gd manner, supporting a more planar metallacrown configuration. For **2**, the H<sub>2</sub>shi ligands replace the benzoates in an analogous manner, to bridge two of the Fe<sup>3+</sup>-Gd<sup>3+</sup> metal pairs through the hydroximate bond as in Fe-O-N-C-O-Gd. However, since there is an additional atom in the sequence the bonding is distorted, bending the ring and ensuring that only two Fe-Gd pairs can be bonded in this Fe-O-N-C-O-Gd manner for **2** rather than the four corresponding Fe-O-C-O-Gd bonds in complex **1**. For **2**, Fe-1 lacks an H<sub>2</sub>Shi ligand bound in this manner, it is replaced by a pyridine molecule.

**Structural images.** All the following images were prepared using Mercury or PyMOL software. Non-coordinated counterions and solvents are in each case omitted for clarity. The common scheme is: Fe, orange; Gd, teal; N, light blue; O, red; C, grey.

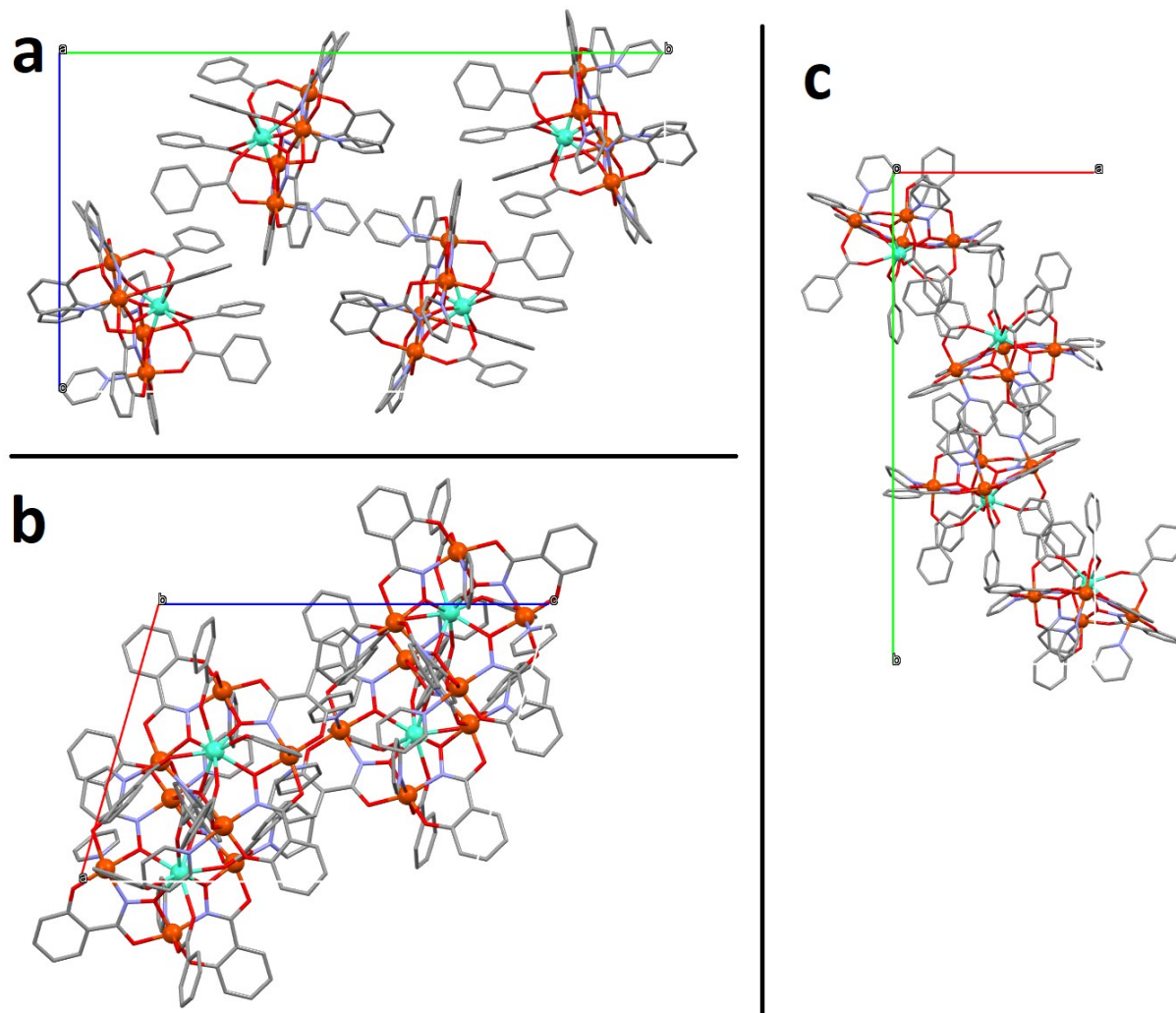


**Figure S1.** Unit cell composition for complex **1** viewed along the a-, b-, and c- axes.

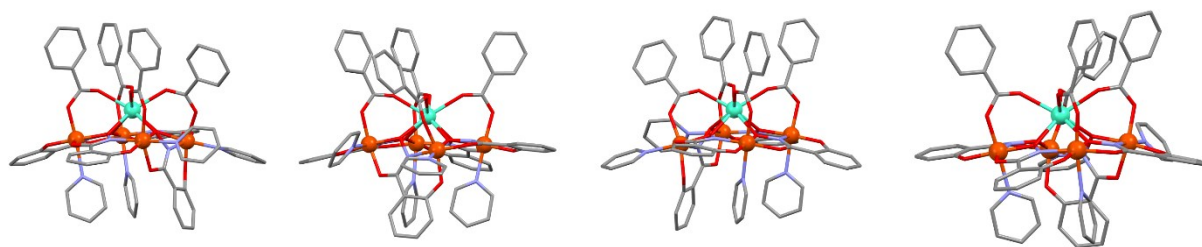


**Figure S2.** Multiple views of complex **1**. Each image is approximately a quarter turn clockwise from the one before.

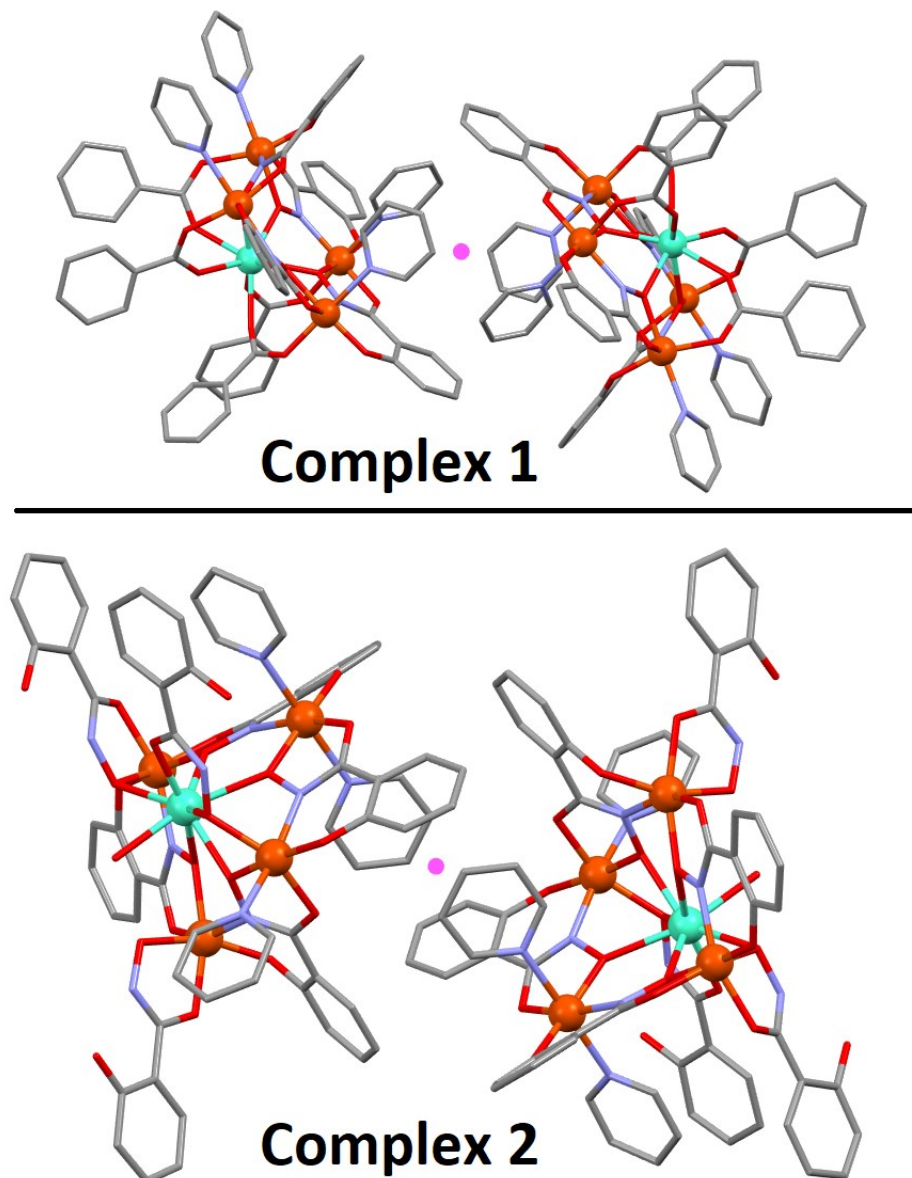


**Figure S3.** View of two isomers of **1** (top) and **2** (bottom). Both **1** and **2** have an inversion center between the two complexes resulting in inversion-center related isomerism. The inversion center is shown as a magenta dot. Complex **1** has, for each unique complex, two planar Fe configurations, one  $\Lambda$  configuration, and one  $\Delta$  configuration. Complex **2** has for one complex: one planar Fe configuration, two  $\Lambda$  configurations, and one  $\Delta$  configuration; and for the inversion-related complex: one planar Fe configuration, one  $\Lambda$  configuration, and two  $\Delta$  configurations. See **Figures S6 and S7**.

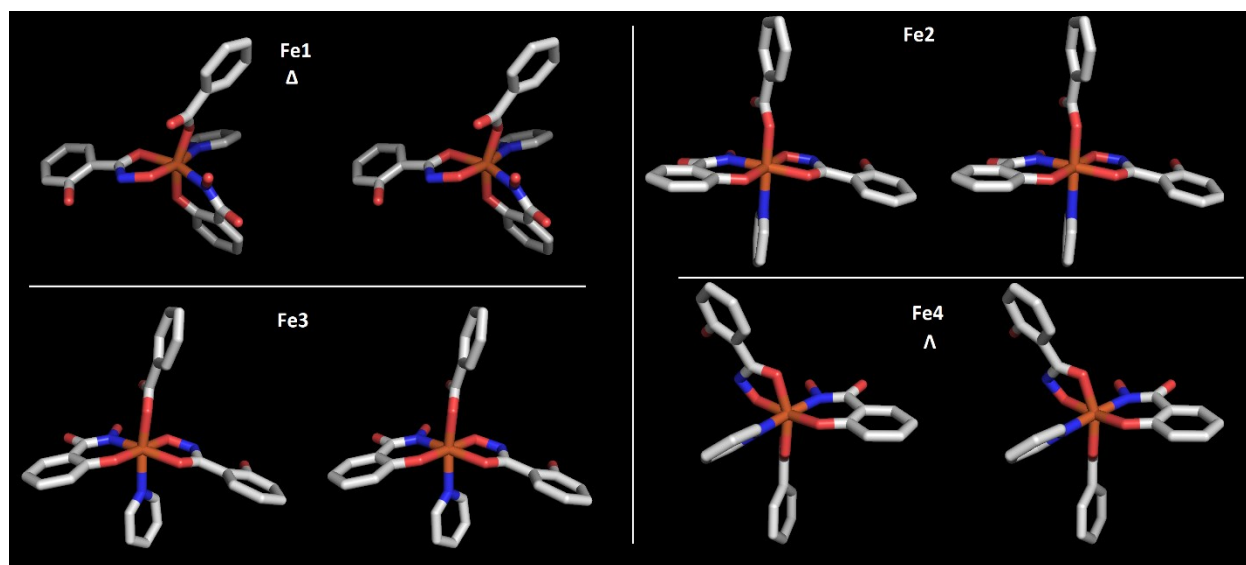


**Figure S4.**  $\Lambda/\Delta$  helical assignments for complex **1** for each of the four irons in each isomer. Each panel represents the walleye stereo view for one of the irons. This figure represents one of the isomers, the other isomer has the opposite assignments. The iron closest to the observer, with the full ligand set, is the one specified by the number. The structure is truncated differently for each image to demonstrate the focused-upon iron's complete ligand set. The irons which are not assigned as  $\Lambda/\Delta$  have planar configurations. This complex has one  $\Lambda$   $\text{Fe}^{3+}$ , one  $\Delta$   $\text{Fe}^{3+}$ , and two planar  $\text{Fe}^{3+}$ .

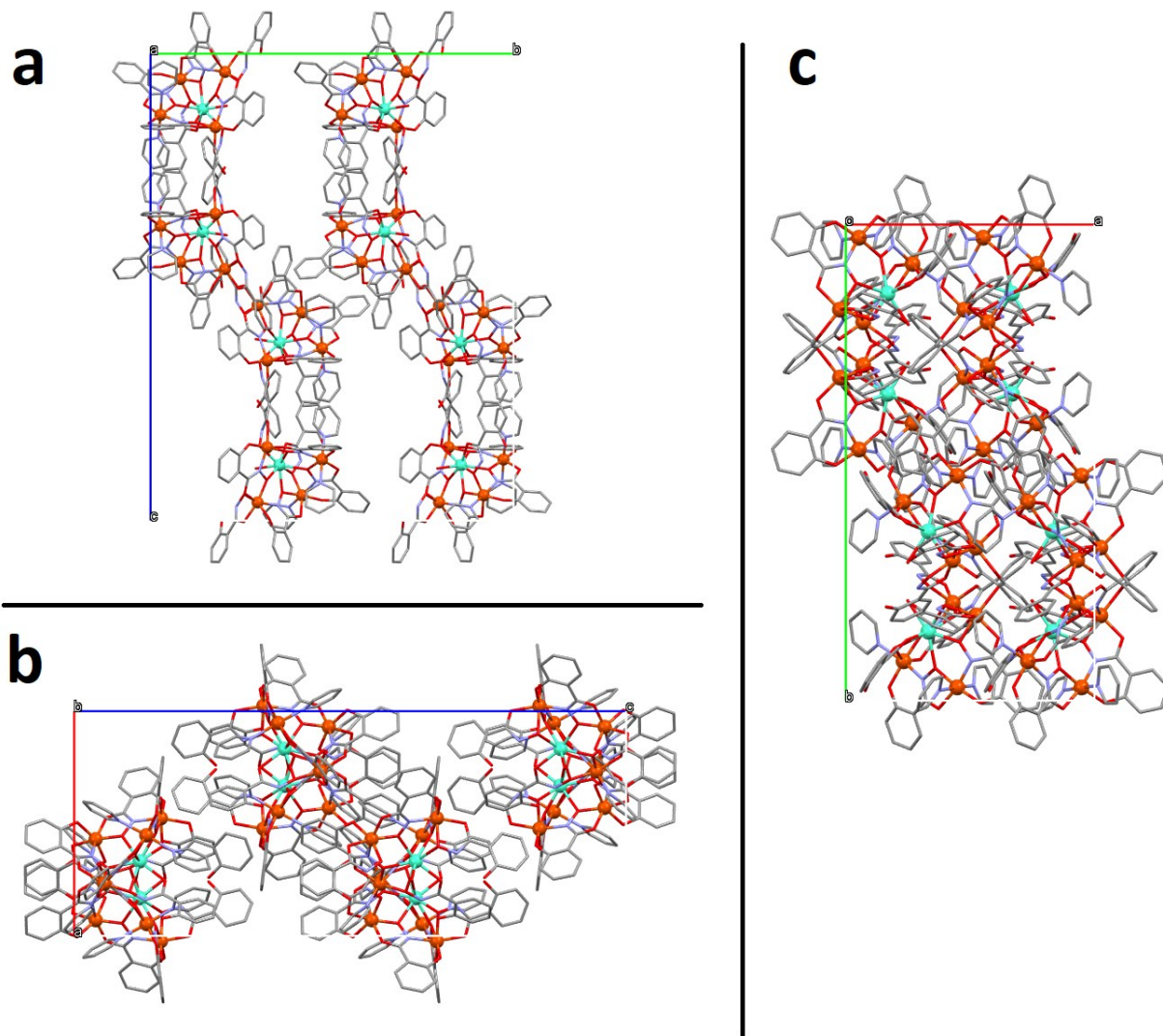


**Figure S5.** Unit cell composition for complex **2** viewed along the a-, b-, and c- axes.

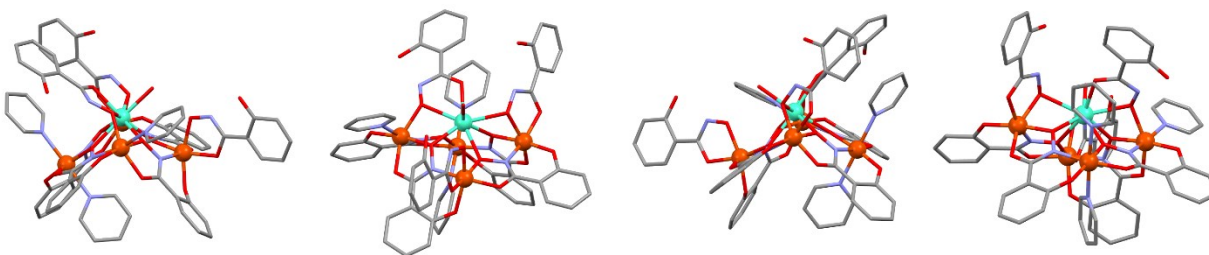


**Figure S6.** Four views of complex **2**. Each image is approximately a quarter turn clockwise from the one before.

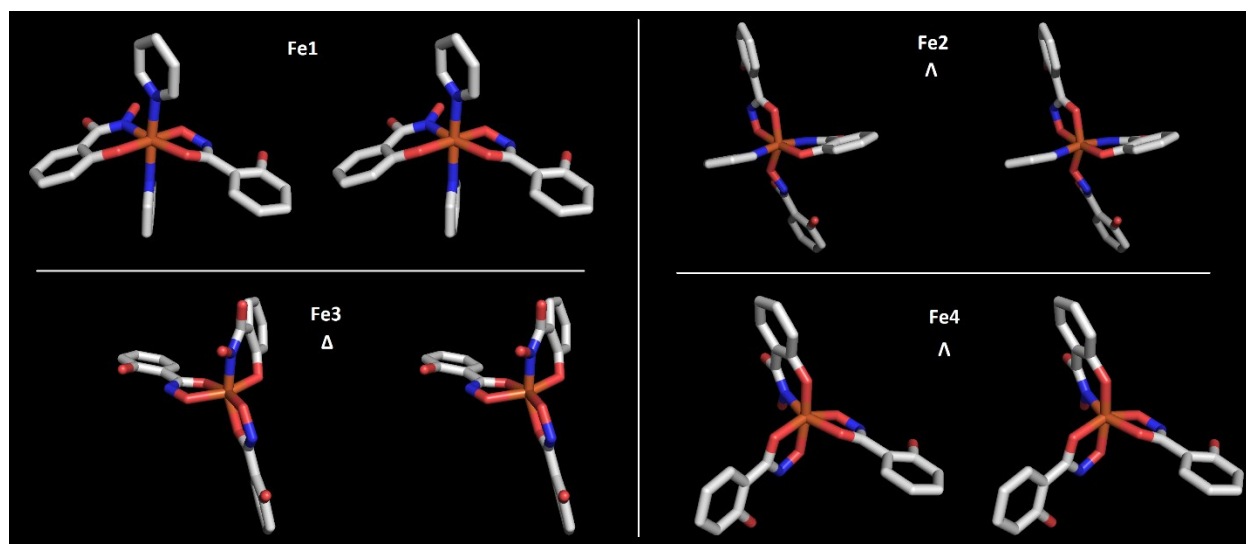


**Figure S7.** Λ/Δ helical assignments for complex **2** for each of the four irons in each isomer. Each panel represents the walleye stereo view for one of the irons. This figure represents one of the isomers, the other isomer has the opposite assignments. The iron closest to the observer, with the full ligand set, is the one specified by the number. The structure is truncated differently for each image to demonstrate the focused-upon iron's complete ligand set. The iron which is not assigned as Λ/Δ has a planar configuration. This complex has two Λ Fe<sup>3+</sup>, one Δ Fe<sup>3+</sup>, and one planar Fe<sup>3+</sup>. The other isomer has the opposite configuration, one Λ Fe<sup>3+</sup>, two Δ Fe<sup>3+</sup>, and one planar Fe<sup>3+</sup>.

**Table S2.** Measurements concerning the primary Gd<sup>3+</sup> coordination sphere distances (Å) for each complex.

	Upper plane <sup>a</sup>				Lower plane <sup>b</sup>			
	Gd-O	Gd-O	Gd-O	Gd-O	Gd-O	Gd-O	Gd-O	Gd-O
<b>1</b>	2.294	2.382	2.336	2.325	2.432	2.398	2.341	2.320
<b>2</b>	2.369	2.484 <sup>c</sup>	2.321	2.485 <sup>c</sup>	2.384	2.298	2.380	2.350

<sup>a</sup>The upper plane are the Gd<sup>3+</sup>- coordinating oxygen atoms furthest from the metallacrown ring. <sup>b</sup>Lower plane are the coordinating oxygen atoms within the metallacrown plane <sup>c</sup>These oxygens are additionally bonded to an Fe<sup>3+</sup> as in Gd<sup>3+</sup>-O-Fe<sup>3+</sup>.

**Table S3.** Measurements concerning the primary Fe<sup>3+</sup> coordination sphere distances (Å) for each complex.

		Equatorial 1 <sup>a</sup>	Equatorial 2 <sup>b</sup>	Equatorial 3 <sup>c</sup>	Equatorial 4 <sup>d</sup>	Upper axial <sup>e</sup>	Lower axial <sup>f</sup>
<b>1</b>	Fe1	Fe-O 2.005	Fe-N 2.012	Fe-O 1.908	Fe-O 1.965	Fe-O 1.970	Fe-N 2.176
	Fe2	Fe-O 1.974	Fe-N 2.055	Fe-O 1.875	Fe-O 1.995	Fe-O 1.972	Fe-N 2.219
	Fe3	Fe-O 2.011	Fe-N 2.034	Fe-O 1.912	Fe-N 2.180	Fe-O 1.953	Fe-O 1.957
	Fe4	Fe-O 1.948	Fe-N 2.053	Fe-N 2.147	Fe-O 2.147	Fe-O 1.955	Fe-O 1.896
<b>2</b>	Fe1	Fe-O 2.010	Fe-N 2.018	Fe-O 1.911	Fe-O 1.976	Fe-N 2.191	Fe-N 2.198
	Fe2	Fe-O 1.990	Fe-N 2.064	Fe-O 1.908	Fe-N 2.162	Fe-O 2.065	Fe-O 2.032
	Fe3	Fe-O 2.030	Fe-N 2.053	Fe-O 2.034	Fe-O 1.976	Fe-O 2.019	Fe-O 1.977
	Fe4	Fe-O 2.020	Fe-N 2.049	Fe-O 1.915	Fe-O 2.022	Fe-O 2.091	Fe-O 2.007

Each Fe<sup>3+</sup> center is a distorted octahedral geometry. <sup>a</sup>These are the Fe-O distances within the metallacrown  $-\text{[Fe-O-N]}_n-$  sequence. <sup>b</sup>These are the Fe-N distances within the metallacrown  $-\text{[Fe-O-N]}_n-$  sequence. <sup>c</sup>This is the atom (closest to) opposite “Equatorial 1.” <sup>d</sup>This is the atom (closest to) opposite “Equatorial 2.” <sup>e</sup>Of the two non-labeled atoms, this is the one closest to the Gd<sup>3+</sup>. <sup>f</sup>the remaining atom.

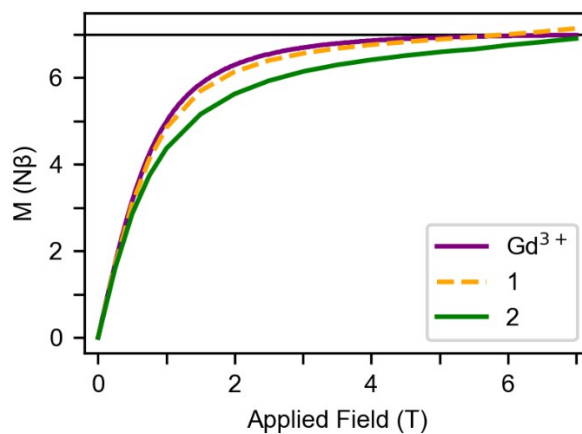


**Figure S8.** Comparison of experimental magnetization data for **1** and **2** at 2K. Brillouin function for an S=7/2 (Gd<sup>3+</sup>) with g = 2 is simulated for reference. Black line plotted at 7 Nβ.

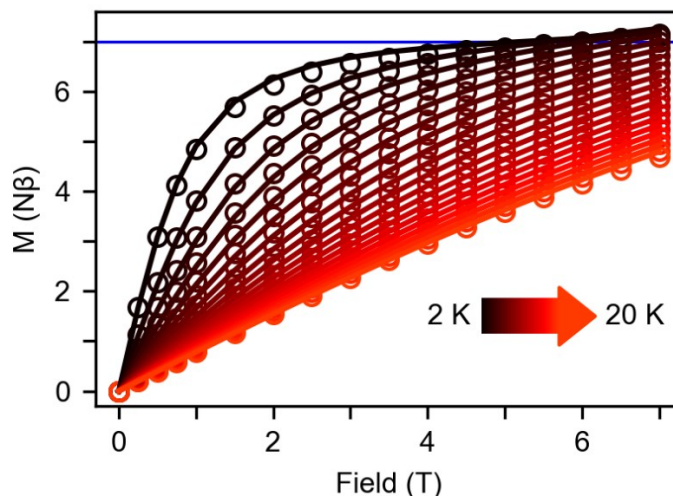


**Figure S9.** Fit of the temperature dependent magnetization data for **1** from 0-7 T, 2-20 K. Data are presented as circles while the fit is the overlaid lines. Fit in conjunction with the magnetic susceptibility data presented in **Figure 4**. Blue line plotted at  $7 N\beta$ .

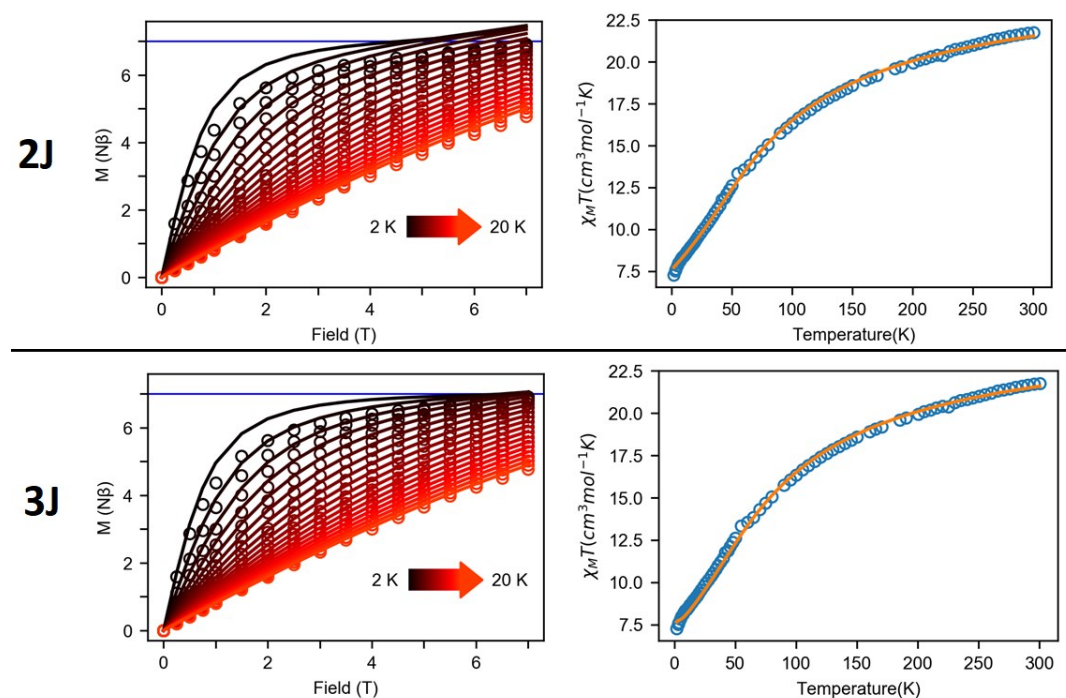


**Figure S10.** Left) Attempted fit of the temperature dependent magnetization data for **2** from 0-7 T, 2-20 K. Right) Corresponding fit of the magnetic susceptibility for **2** data with 2000 Oe applied field. The top plots are using a 2-J component spin Hamiltonian. The bottom plots are using a 3-J component spin Hamiltonian. For 2J, the best parameters obtained were  $J_1 = -7.76 \text{ cm}^{-1}$  and  $J_2 = -0.18 \text{ cm}^{-1}$ . For 3J, the best parameters obtained were  $J_1 = -7.32 \text{ cm}^{-1}$ ,  $J_2 = -0.17 \text{ cm}^{-1}$ , and  $J_2' = -0.74 \text{ cm}^{-1}$ . However, similar fits were obtained with  $J_1$  ranging from  $\sim -9$  to  $-7 \text{ cm}^{-1}$  and  $J_2$  and  $J_2'$  ranging from ca.  $-1.0$  to  $+0.2 \text{ cm}^{-1}$ . Due to the inability to pinpoint a single best fit, as well as the incongruity of the fit with the magnetization data, a fitted spin Hamiltonian for complex **2** is not presented in the main text.

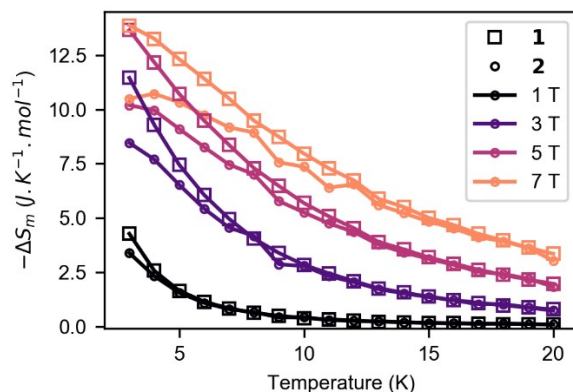


**Figure S11.** Temperature dependent magnetic entropy change (per mole) in the range 3-20 K. Plot obtained from a numerical evaluation of the data in **Figure 5** according to **eqn 2b** with integration from 0 to 1, 3, 5, and 7 Tesla. Complex **1** data shown as squares, complex **2** as circles. Data is presented in the mass basis in **Figure 6**.

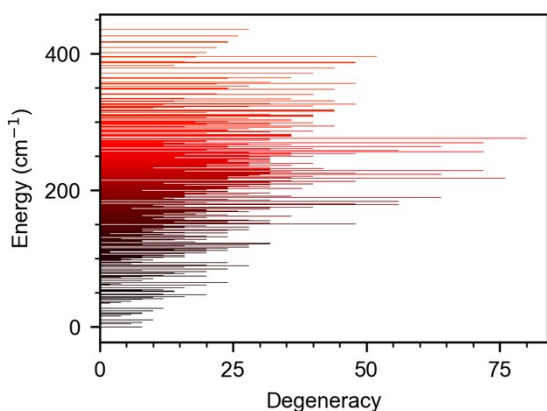


**Figure S12.** Energy levels determined via fitting the spin Hamiltonian to the data for **1** by the PHI package. These figures plot the energy of each spin state as well as the level's degeneracy in zero applied magnetic fields. Energy levels from 0-450  $\text{cm}^{-1}$ .

### Calculating the magnetic entropy at 2K

By using the zero-field energy levels calculated from the spin Hamiltonian, one can calculate the magnetic entropy for a particular temperature using the partition function for the system. If considering only magnetic energy levels, the partition function ( $Q$ ) is given by:

$$\text{eqn S1: } Q = \sum_{i=1}^M g_i e^{-\varepsilon_i/k_B T}$$

Where  $\varepsilon_i$  is the energy of each level relative to the ground state,  $g_i$  is the degeneracy of each level ( $g_i = 2S+1$ , where  $S$  is the spin for a given level),  $k_B$  is the Boltzmann constant, and  $T$  is the temperature of the system. The sum is over all energy levels ( $M$ ). From the partition function, the molar magnetic entropy ( $S_m$ ) can be calculated as:

$$\text{eqn S2: } S_m = N k_B \ln Q$$

Where  $N$  is Avogadro's number. The population of each energy level can also be determined via:

$$\text{eqn S3: } p_i = \frac{1}{Q} g_i e^{-\varepsilon_i/k_B T}$$

During magnetization, optimally one energy level will be well-separated from the others via the Zeeman effect, such that only a single state is occupied and  $S_m^{\text{applied field}} = 0$ . This signifies that  $\Delta S_m = S_m^{\text{applied field}} - S_m^{\text{zero field}} = 0 - Nk_B \ln Q$ . When only considering the ground state (of spin  $S_{\text{ground}}$ ),  $Q$  simplifies to  $g_{\text{ground}}$  such that  $-\Delta S_m = Nk_B \ln g_{\text{ground}}$  [ $-\Delta S_m = Nk_B \ln(2S_{\text{ground}} + 1)$ ]. One can expect  $-\Delta S_m$  to be smaller than this when the magnetic moment is not fully saturated during magnetization (i.e.,  $S_m^{\text{applied field}} \neq 0$ ). One can expect  $-\Delta S_m$  to be larger than this when low-lying excited states can be populated at zero field at the operating temperature ( $\sim 2\text{K}$  for molecular MCE materials) and contribute to  $S_m$ . This demonstrates the usefulness of having low lying excited states which can be thermally occupied to increase the entropy beyond  $S_m = Nk_B \ln(2S_{\text{ground}} + 1)$ . But since molecular MCE materials operate optimally at minimal temperatures, these states must be extremely low-lying to become occupied, therein outlining a challenge in improving molecular MCE materials.

If the energy levels and their degeneracy can be calculated (e.g. from a spin Hamiltonian), the  $S_m^{\text{zero field}}$  can be calculated ( $S_m^{\text{CALC}}$ , see Supporting Information). The upper limit of  $-\Delta S_m$  can be estimated by assuming that only one state is occupied during magnetization, since  $\Delta S_m = S_m^{\text{applied field}} - S_m^{\text{zero field}}$  (in practice it will likely be less as the moment will not be fully saturated into one single state). This yields the upper limit  $-\Delta S_m^{\text{CALC}}$  (upper limit) =  $S_m^{\text{zero field}} (S_m^{\text{CALC}}) = Nk_B \ln Q$ . Higher entropy at zero field should correspond then to a higher  $-\Delta S_m$ .

**Table S6. A collection of structural and magnetic parameters relating to metallacrown complexes**

No.	Metallacrown	$M_2^{n+}\text{-N-O-}M_2^{n+}$ torsion ( $^\circ$ )	$M_1^{n+}\text{-O-}M_2^{n+}$ angle ( $^\circ$ )	$J_1$ ( $\text{cm}^{-1}$ )	$J_2$ ( $\text{cm}^{-1}$ )	$S_T$	Ground Spin	ref
1	$\text{Gd}^{3+}[\text{12-MC}_{\text{Fe}^{\text{III}}_{\text{N}(\text{shi})}\text{-4}}$	$166.9 \pm 9.1$	$119.8 \pm 2.3$	-7.5	-0.71	27/2	7/2	-
3	$\text{Fe}^{3+}[\text{9-MC}_{\text{Fe}^{\text{III}}_{\text{N}(\text{shi})}\text{-3}]$ -1	152.2	113.8	-4.5	-24.9	10	5	2
4	$\text{Fe}^{3+}[\text{9-MC}_{\text{Fe}^{\text{III}}_{\text{N}(\text{shi})}\text{-3}]$ -2	150.5	114.7	-6.4	-28.0	10	5	2
5	$\text{Cu}^{2+}[\text{12-MC}_{\text{Fe}^{\text{III}}_{\text{N}(\text{shi})}\text{-4}]$	$172.4 \pm 0.5$	$123.8 \pm 0.3$	-7.6	-98.4	21/2	11/2	6

All complexes were fitted to a 2-J component spin-only Hamiltonian.  $S_T$  is the total spin, taken by adding all the spins for each paramagnetic ion in the complex if considered uncoupled. The ground spin is the spin present in the energy diagram dictated by the  $J_1$  and  $J_2$  parameters. All exchange parameters were corrected to the notation given in **eqn 1**, such that  $J_1$  refers to nearest-neighbor ring coupling ( $M_2^{n+}\text{-N-O-}M_2^{n+}$ ) and  $J_2$  refers to ring metal-central ion coupling ( $M_1^{n+}\text{-O-}M_2^{n+}$ ).  $M_1^{n+}$  refers to the centrally bound ion,  $M_2^{n+}$  refers to the ring metal ions, here fitted as if magnetically equivalent in each case.  $M_2^{n+}\text{-N-O-}M_2^{n+}$  torsion is the torsion angle in that bond sequence. The value is the average measurement of all such bonds, and the “uncertainty” comes from the standard deviation amongst these measurements. If no uncertainty is presented, all given bonds are crystallographically equivalent. The  $M_1^{n+}\text{-O-}M_2^{n+}$  angle is described similarly.

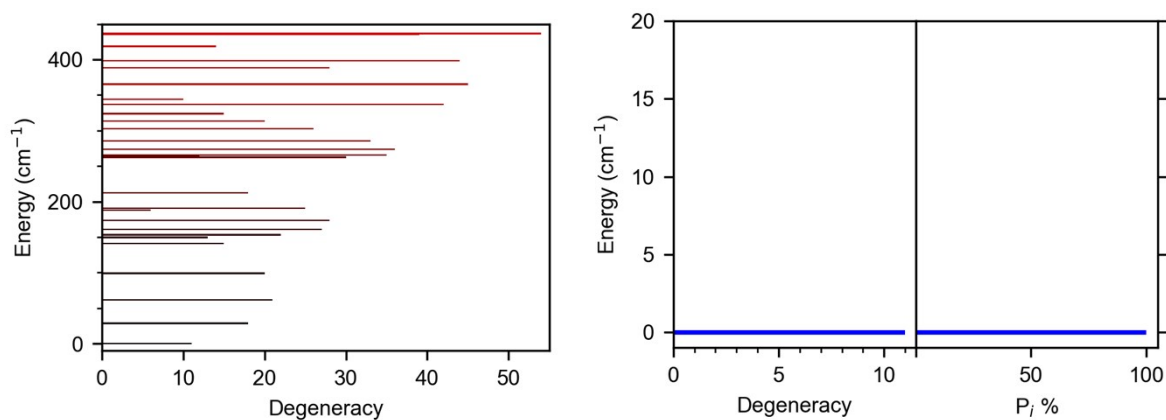


**Figure S13.** Simulation of the energy levels of  $\text{Fe}^{3+}[\text{9-MC}_{\text{Fe}^{\text{III}}_{\text{N}(\text{shi})}\text{-3}]$ -1 (**3**) using the Hamiltonian

$$\hat{H} = -J_1(\mathcal{S}_2 \cdot \mathcal{S}_3 + \mathcal{S}_3 \cdot \mathcal{S}_4 + \mathcal{S}_4 \cdot \mathcal{S}_2) - J_2(\mathcal{S}_1 \cdot \mathcal{S}_2 + \mathcal{S}_1 \cdot \mathcal{S}_3 + \mathcal{S}_1 \cdot \mathcal{S}_4) + \beta \sum_{i=1}^N \mathcal{S}_i \cdot g_i \cdot \vec{B}$$

and the parameters ( $g=1.97$ ,  $J_1=-6.4 \text{ cm}^{-1}$ ,  $J_2=-28.0 \text{ cm}^{-1}$ , including an intermolecular interaction parameter:  $zJ=-0.69 \text{ cm}^{-1}$ ) taken from the original report of the complex.<sup>2</sup> The left figure shows the

energy levels from 0-450  $\text{cm}^{-1}$  and the right figure shows the energy levels from 0-20  $\text{cm}^{-1}$ , and their populations at 2 K calculated according to eqns S1 and S3. The calculated magnetic entropy at 2K:  $S_m^{\text{CALC}}=19.94 \text{ JK}^{-1}\text{mol}^{-1}$  was determined as described above using these energy levels and eqns S1 and S2.

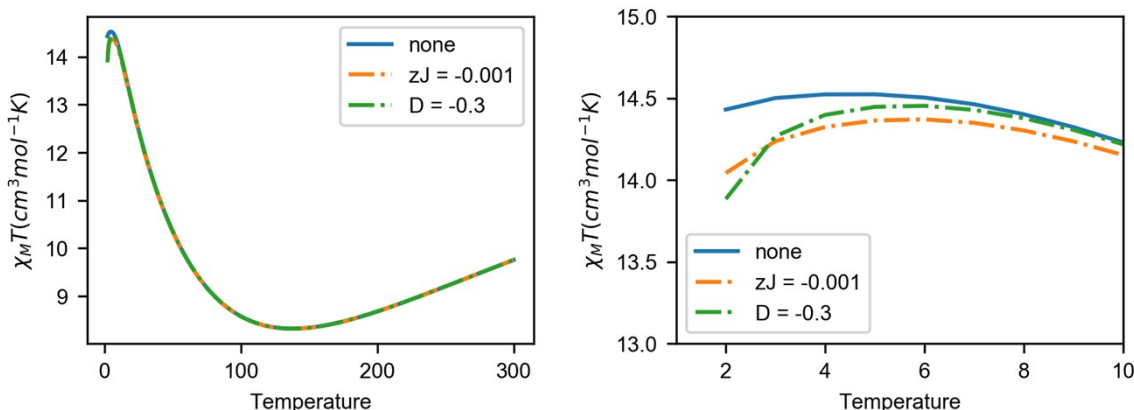


**Figure S14.** Simulation of the magnetic susceptibility of the complex  $\text{Fe}^{3+}[\text{9-MC}_{\text{Fe}^{\text{III}}_{\text{N}(\text{shi})}\text{-3]}\cdot 2$  (4) described by Chow et al.<sup>2</sup> The right figure focuses on the low-temperature region. The  $\chi T$  is simulated using the previously described parameters ( $g=1.97$ ,  $J_1=-6.4 \text{ cm}^{-1}$ ,  $J_2=-28.0 \text{ cm}^{-1}$ ,  $D=-0.3 \text{ cm}^{-1}$ ) and the Hamiltonian

$$\hat{H} = -J_1(\hat{S}_2 \cdot \hat{S}_3 + \hat{S}_3 \cdot \hat{S}_4 + \hat{S}_4 \cdot \hat{S}_2) - J_2(\hat{S}_1 \cdot \hat{S}_2 + \hat{S}_1 \cdot \hat{S}_3 + \hat{S}_1 \cdot \hat{S}_4) + D\left(S_z^2 - \frac{S(S+1)}{3}\right) + \beta \sum_{i=1}^N \hat{S}_i \cdot g_i \cdot \vec{B}$$

in green. The blue curve removes the axial term (i.e.,  $D=0$ ); while the orange curve removes the axial term and adds an intermolecular interaction parameter,  $zJ=-0.001 \text{ cm}^{-1}$ . The axial field treatment ( $D=-0.3 \text{ cm}^{-1}$ , green curve) and the intermolecular interaction ( $zJ=-0.001$ , orange curve) produce similar  $\chi T$  behavior. However, the intermolecular treatment yields behavior more in-line with the observed MCE behavior (see text). The simulated energy levels for these treatments are given in **Figures S14-S15**.

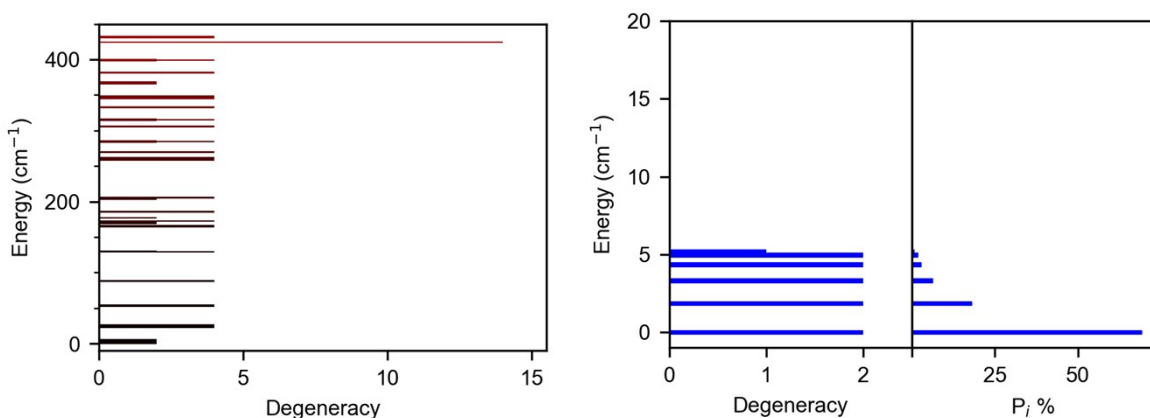


**Figure S15.** Simulation of the energy levels of  $\text{Fe}^{3+}[\text{9-MC}_{\text{Fe}^{\text{III}}_{\text{N}(\text{shi})}\text{-3]}\cdot 2$  (4) using the Hamiltonian described in **Figure S14** and the parameters ( $g=1.97$ ,  $J_1=-6.4 \text{ cm}^{-1}$ ,  $J_2=-28.0 \text{ cm}^{-1}$ ,  $D=-0.3 \text{ cm}^{-1}$ ). The left figure shows the energy levels from 0-450  $\text{cm}^{-1}$  and the right figure shows the energy levels from 0-20  $\text{cm}^{-1}$ , and their populations at 2 K calculated according to eqns S1 and S3. The calculated magnetic

entropy at 2K:  $S_m^{\text{CALC}}=8.79 \text{ JK}^{-1}\text{mol}^{-1}$  was determined as described above using these energy levels and eqns S1 and S2.

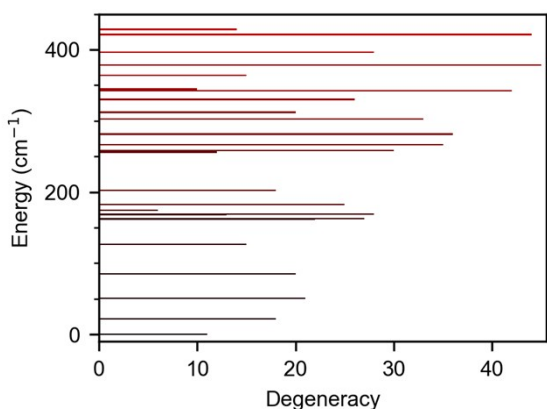


**Figure S16.** Simulation of the energy levels of  $\text{Fe}^{3+}[\text{9-MC}_{\text{Fe}^{\text{III}}\text{N}(\text{shi})\text{-3}}\text{-2}]$  (**4**) using the Hamiltonian described in **Figure S14** and the parameters ( $g=1.97$ ,  $J_1=-6.4 \text{ cm}^{-1}$ ,  $J_2=-28.0 \text{ cm}^{-1}$ ,  $D=0$ ,  $zJ=-0.001 \text{ cm}^{-1}$ ). The left figure shows the energy levels from 0-450  $\text{cm}^{-1}$  and the right figure shows the energy levels from 0-20  $\text{cm}^{-1}$ , and their populations at 2 K calculated according to **eqns S1 and S3**. The calculated magnetic entropy at 2K:  $S_m^{\text{CALC}}=19.94 \text{ JK}^{-1}\text{mol}^{-1}$  was determined as described above using these energy levels and **eqns S1 and S2**.

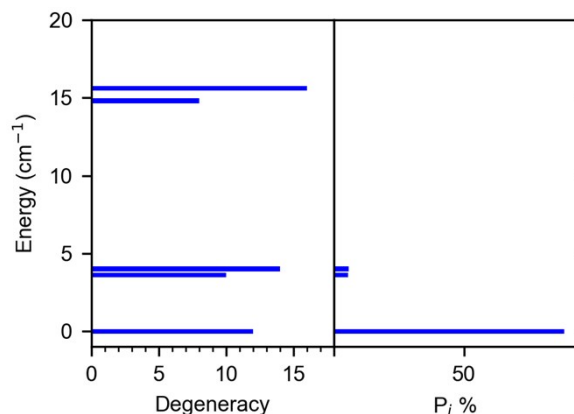
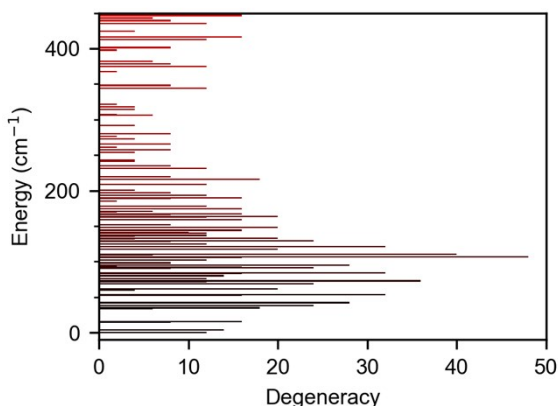


**Figure S17.** Simulation of the energy levels of  $\text{Cu}^{2+}[\text{12-MC}_{\text{Fe}^{\text{III}}\text{N}(\text{shi})\text{-4}}]$  (**5**) using **eqn 1** and the parameters taken from the original report of the complex.<sup>6</sup> The left figure shows the energy levels from 0-450  $\text{cm}^{-1}$  and the right figure shows the energy levels from 0-20  $\text{cm}^{-1}$ , and their populations at 2 K calculated according to **eqns S1 and S3**. The calculated magnetic entropy at 2K:  $S_m^{\text{CALC}}=21.66 \text{ JK}^{-1}\text{mol}^{-1}$  was determined as described above using these energy levels and **eqns S1 and S2**.

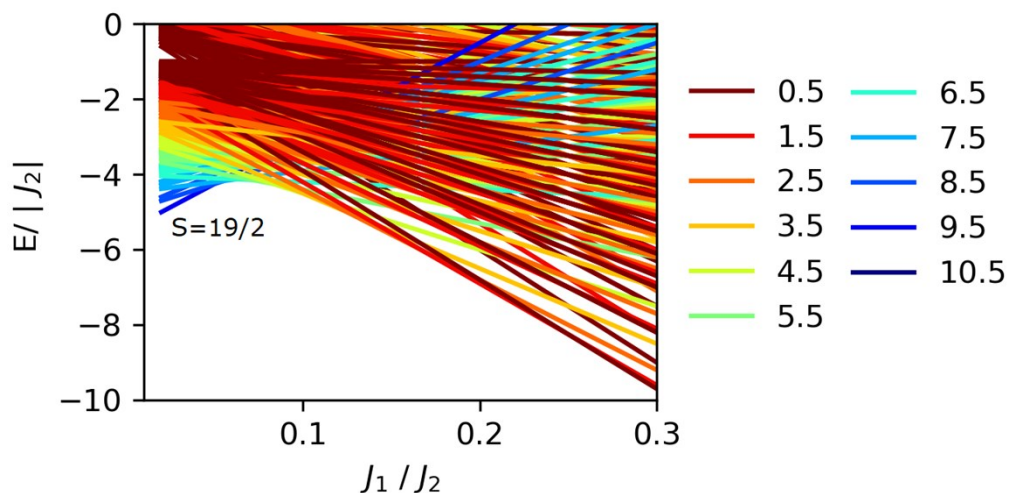


**Figure S18.** Lower portion of the Energy diagram for the spin states of  $\text{Cu}^{3+}\text{Fe}^{3+}_4$  plotted as  $E/|J_2|$  vs  $J_1/J_2$ . For an  $S=19/2$  state, a  $J_1/J_2$  ratio  $<$  ca. 0.05 is necessary. The experimental ratio  $J_1/J_2$  is 0.077, indicating an  $S=11/2$  ground state.

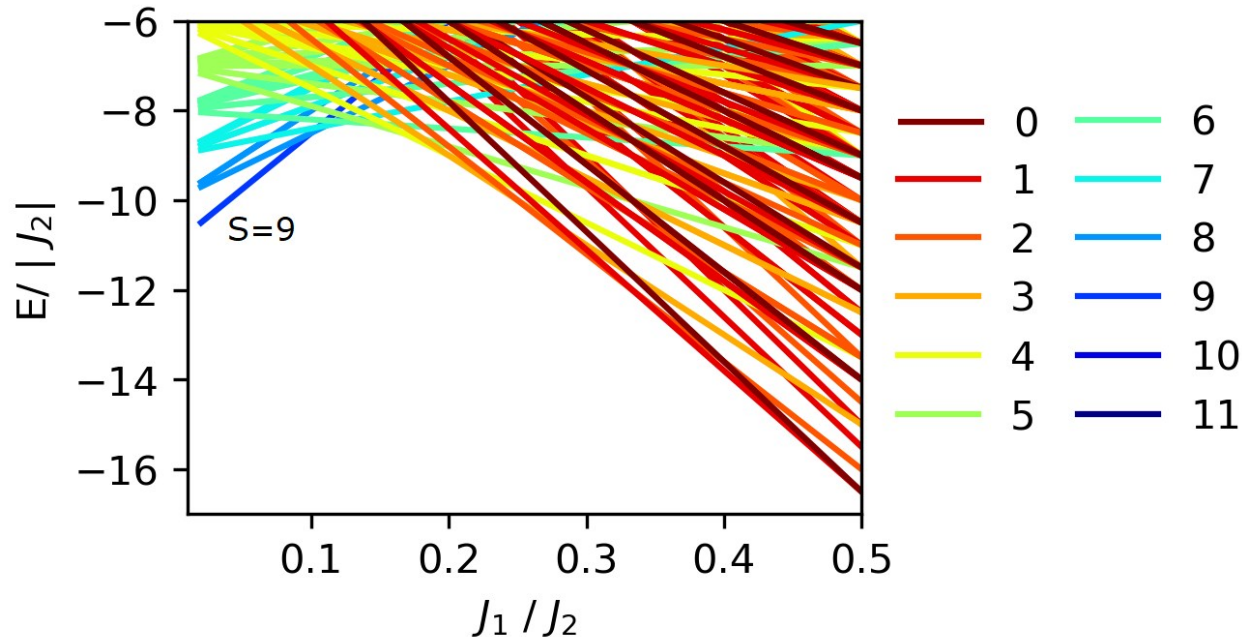


**Figure S19.** Lower portion of the Energy diagram for the spin states of  $\text{Ni}^{2+}\text{Fe}^{3+}_4$  plotted as  $E/|J_2|$  vs  $J_1/J_2$ . For an  $S=9$  state, a  $J_1/J_2$  ratio  $<$  ca. 0.099 is necessary.

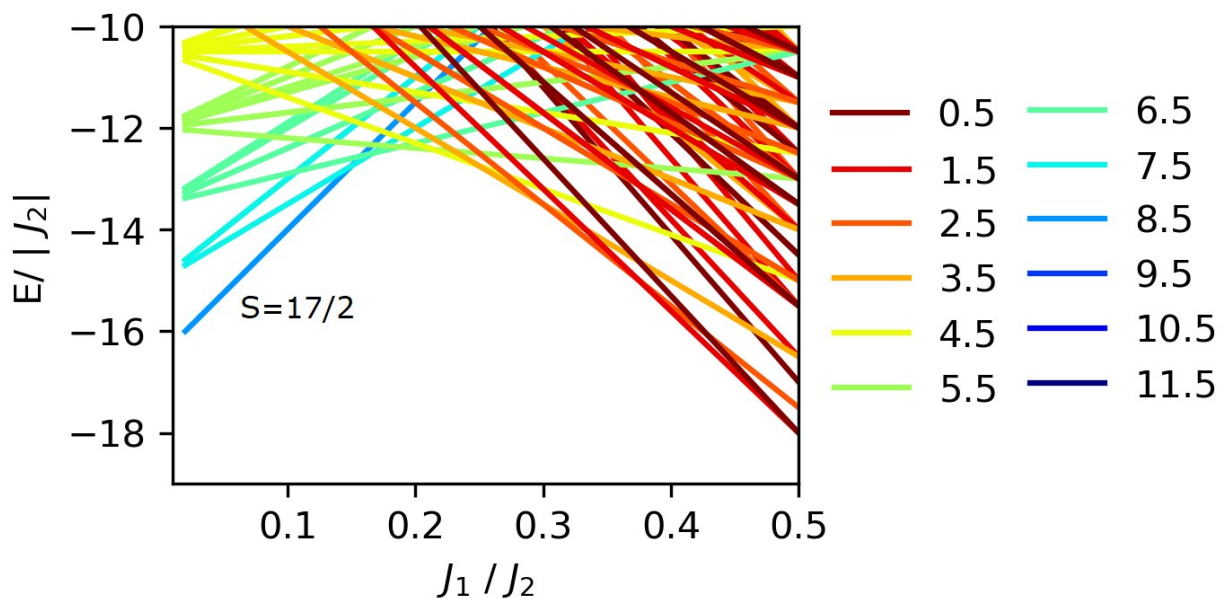


**Figure S20.** Lower portion of the Energy diagram for the spin states of  $\text{Co}^{2+}\text{Fe}^{3+}_4$  plotted as  $E/|J_2|$  vs  $J_1/J_2$ . For an  $S=17/2$  state, a  $J_1/J_2$  ratio  $<$  ca. 0.147 is necessary.

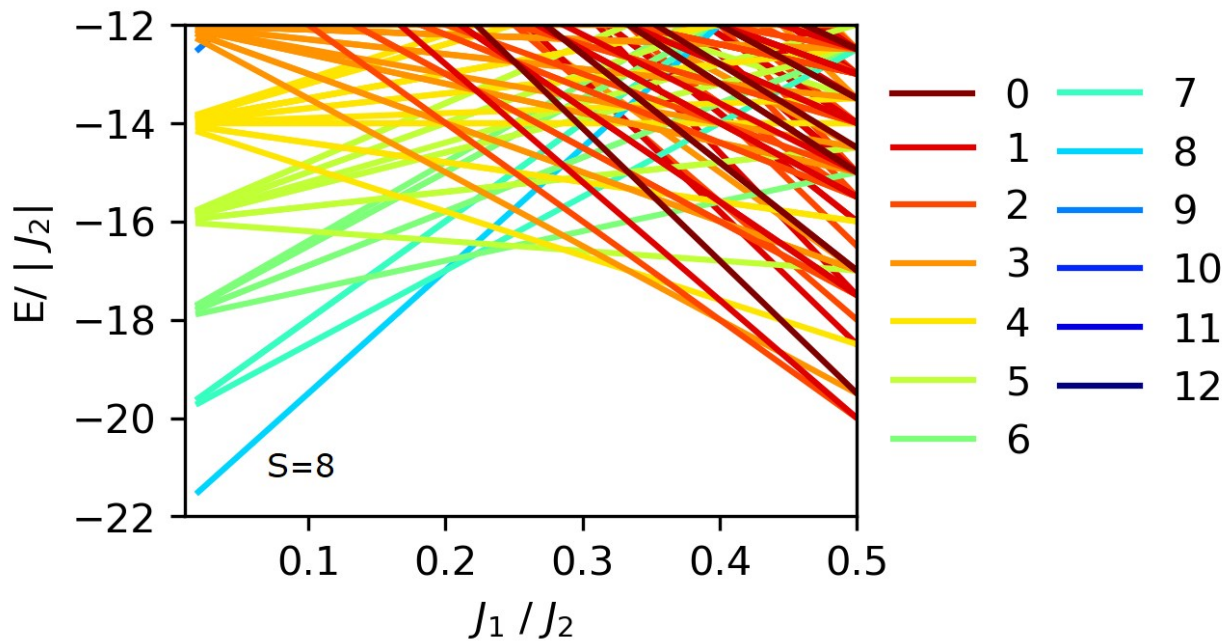


**Figure S21.** Lower portion of the Energy diagram for the spin states of  $\text{Mn}^{3+}\text{Fe}^{3+}_4$  plotted as  $E/|J_2|$  vs  $J_1/J_2$ . For an  $S=8$  state, a  $J_1/J_2$  ratio  $<$  ca. 0.195 is necessary.

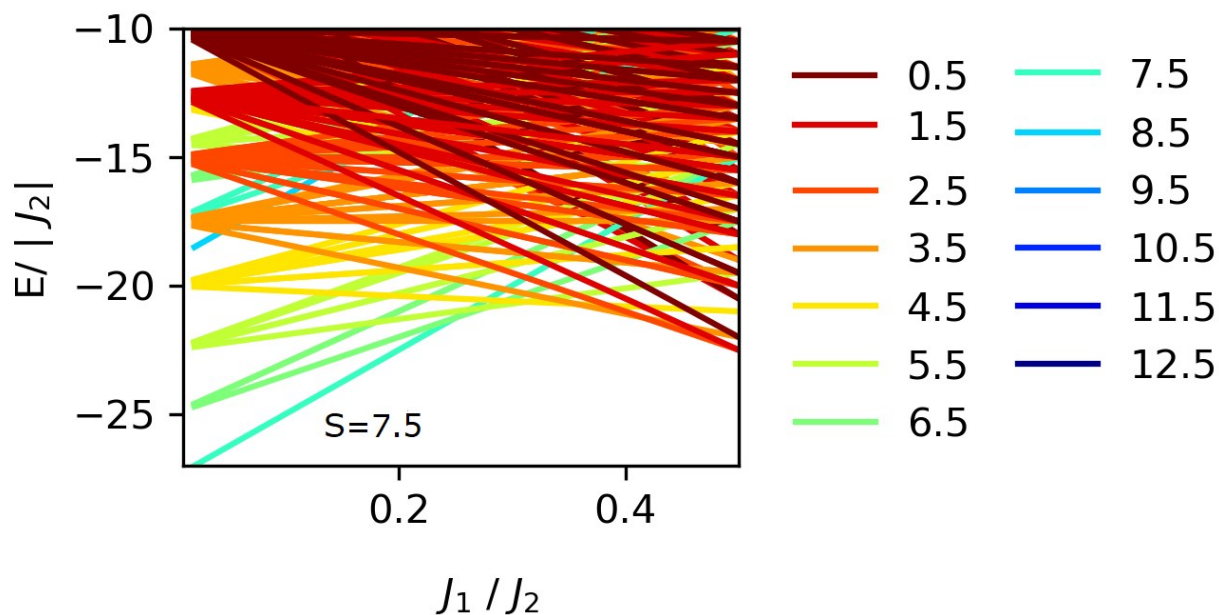


**Figure S22.** Lower portion of the Energy diagram for the spin states of  $\text{Fe}^{3+}\text{Fe}^{3+}_4$  plotted as  $E/|J_2|$  vs  $J_1/J_2$ . For an  $S=15/2$  state, a  $J_1/J_2$  ratio  $<$  ca. 0.245 is necessary.

## REFERENCES

- (1) Lou, T.; Yang, H.; Zeng, S.; Li, D.; Dou, J. A New Family of Heterometallic LnIII [12-MCFe IIIIn(Shi)-4] Complexes: Syntheses, Structures and Magnetic Properties. *Crystals* **2018**, *8* (5). <https://doi.org/10.3390/cryst8050229>.
- (2) Chow, C. Y.; Guillot, R.; Rivière, E.; Kampf, J. W.; Mallah, T.; Pecoraro, V. L. Synthesis and Magnetic Characterization of Fe(III)-Based 9-Metallacrown-3 Complexes Which Exhibit Magnetorefrigerant Properties. *Inorg. Chem.* **2016**, *55* (20), 10238–10247. <https://doi.org/10.1021/acs.inorgchem.6b01404>.
- (3) Lah, M. S.; Kirk, M. L.; Hatfield, W.; Pecoraro, V. L. The Tetranuclear Cluster  $\text{Fe}^{\text{III}}[\text{Fe}^{\text{III}}(\text{Salicylhydroximato})(\text{MeOH})(\text{Acetate})_3]$  Is an Analogue of  $\text{M}^{3+}(9\text{-Crown-3})$ . *J. Chem. Soc. Chem. Commun.* **1989**, No. 21, 1606–1608. <https://doi.org/10.1039/c39890001606>.
- (4) Kessissoglou, D. P.; Kampf, J.; Pecoraro, V. L. Compositional and Geometrical Isomers of 15-Metallacrowns-5 Complexes. *Polyhedron* **1994**, *13* (9), 1379–1391. [https://doi.org/10.1016/S0277-5387\(00\)81704-0](https://doi.org/10.1016/S0277-5387(00)81704-0).
- (5) Afrati, T.; Dendrinou-Samara, C.; Zaleski, C. M.; Kampf, J. W.; Pecoraro, V. L.; Kessissoglou, D. P. Synthesis and Structure of  $[18\text{-MC}_{\text{CuII}(\text{N})\text{Pko}}\text{-6}]^{6+}$ : A New Member of Anion Encapsulating Metallamacrocycles. *Inorg. Chem. Commun.* **2005**, *8* (12), 1173–1176. <https://doi.org/10.1016/j.inoche.2005.09.024>.
- (6) Happ, P.; Rentschler, E. Enforcement of a High-Spin Ground State for the First 3d Heterometallic 12-Metallacrown-4 Complex. *Dalt. Trans.* **2014**, *43* (41), 15308–15312. <https://doi.org/10.1039/c4dt02275k>.